Hydrodynamic Imaging using an all-optical 2D Artificial Lateral Line

Wolf, Berend; van Netten, Sietse

Published in:
2019 IEEE Sensors Applications Symposium (SAS)

DOI:
10.1109/SAS.2019.8706030

This full text paper was peer-reviewed at the direction of IEEE Instrumentation and Measurement Society prior to the acceptance and publication.

Hydrodynamic Imaging using an all-optical 2D Artificial Lateral Line

Ben J. Wolf
Bernoulli Institute
dept. of Artificial Intelligence
University of Groningen
Groningen, Netherlands
b.j.wolf@rug.nl

Sietse M. van Netten
Bernoulli Institute
dept. of Artificial Intelligence
University of Groningen
Groningen, Netherlands
s.m.van.netten@rug.nl

***Abstract*—Fish and amphibians can sense their hydrodynamic environment via fluid flow sensing organs, called lateral lines. Using this lateral line they are able to detect disturbances in the hydrodynamic near field which enables hydrodynamic imaging, i.e. obstacle detection. Via two experiments we demonstrate a novel artificial lateral line of four bio-inspired 2D fluid flow sensors and show that the measurements of the enacted sensors agree with an established hydrodynamic model. These measurements from the array are then used to localize both vibrating and unidirectionally moving objects using an artificial neural network in a bounded area of 36 by 11 cm which extends beyond the area directly in front of the sensor array. In this area, the average Euclidean localization error is 1.3 cm for a vibrating object, while for moving a object it is on average 3.3 cm.**

***Index Terms*—artificial lateral line, hydrodynamics, neural networks, sensor array, extreme learning machine**

I. Introduction

The development of our sensory array is based on a biomimetic approach as the design is directly inspired by a sensory modality used for flow detection by aquatic vertebrates; fish and amphibians have the unique ability to detect and localize moving and vibrating underwater objects [1]. Along the head and trunk they have an array of discrete mechanical sensors at their disposal called neuromasts. With these neuromasts they can perceive the local water motion – or flow – relative to their body.

Artificial lateral lines (ALLs) provide a passive sensor system that works in the hydrodynamic near field which does not rely on vision or an active beacon. Other technologies, e.g. sonar, do require an active beacon which is detectable and can affect marine ecosystems.

ALLs can be used in two modes. It can be used to help autonomous underwater vehicles (AUVs) safely navigate murky waters in terms of obstacle detection, bridging the gap between touch and vision. Secondly, the system could be used in harbors and other waterways to passively monitor marine traffic or marine life.

Several implementations of ALLs exist [2]. Most implementations are scaled down versions called mechanical micro sensors (MEMs), which make use of piezo-strain sensing, while others use pressure sensors or optical levers with LEDs [3]. The present work demonstrates the first use of all-optical sensors in an ALL, which does not rely on electrical signals and could therefore be more reliable in operation. In addition, some ALLs [4], [5] show varying sensor orientations, allowing to partly capture the information of fluid flow perpendicular to the array. The presented sensor array is one of the first artificial lateral lines that combines the parallel and orthogonal velocity profile components in single measurement points, which has been shown to be beneficial for location estimation in simulation [6].

In this paper, we demonstrate hydrodynamic imaging [7], i.e. the ability to detect an object near the sensor array, via two benchmarks. The first benchmark task sets out to localize a stationary vibrating (dipole) object positioned at discrete locations, while the second task involves tracking and localizing a unidirectionally moving object. To estimate the location from the sensor data, we make use of a fast artificial neural network architecture. This type of neural network is also used in [6], [8], which are both simulation studies for continuous moving objects; whereas the current study aims to demonstrate hydrodynamic imaging via real-world experiments.

The rest of the paper is structured as follows: In section II we further describe the nature of velocity profiles, the sensors, and other relevant literature. In section III and IV, we present an experiments for localizing a vibrating object and a moving object respectively. We discuss our findings in section V and conclude in section VI.

II. background

A. Bioinspiration

The fish lateral line is made up from two types of mechanosensory neuromasts, each with their own beneficial physical properties to help the fish perceive freestream (DC) and dynamic or oscillatory (AC) flow [1]. Superficial neuromasts (SNs) are present on the fish bodies' surface and are in direct contact with the surrounding. They are tailored to perceive steady flow i.e. fluid velocity. Canal neuromasts (CNs) are embedded in subdermal canals and therefore shielded from the DC flow and tailored towards AC fluid flow.

This research has been supported by the Lakhsmi project that has received funding from the European Union's Horizon 2020 research and innovation program under grant agreement No 635568.

978-1-5386-7713-1/19/$31.00 ©2019 IEEE

The perceived local fluid flow can be concatenated to a spatial velocity profile through combining information from other CNs and SNs in the lateral line system, which augments the fish sensory perception [9]. In behavioral fish experiments, the lateral line has been shown to be instrumental in many specific behaviors, for instance: prey detection, predator avoidance, schooling behavior, and spatial orientation [9]. The sensors described in this work are used as superficial neuromasts.

B. Velocity profiles

In previous research, theoretical models are described that predict velocity profiles (i.e. the local fluid velocities at each sensor unit on a given time) along a 1D array. Here, an object is either vibrating in a direction with a specific angle with respect to the array [10]–[13] or moving in a specific direction [14]. Using these models based on non-viscous flow around a sphere, velocity profiles can be modeled for different locations and movement directions for a spherical object located at coordinate (b, d).

The local fluid velocity component parallel to the array, v_x, on position s on the sensor array is given by a combination of two wavelets [11]. The magnitude of the velocity profile scales with the radius of a sphere a, its speed magnitude W, and its distance d to the array.

$$v_x = \frac{Wa^3}{2d^3}(\Psi_\mathrm{o}\sin\varphi - \Psi_\mathrm{e}\cos\varphi). \tag{1}$$

The angle of the object with respect to the sensor array is φ. The even wavelet Ψ_e and odd wavelet Ψ_o are described by:

$$\Psi_\mathrm{e} = \frac{1-2\rho^2}{(1+\rho)^{\frac{5}{2}}}, \tag{2}$$

$$\Psi_\mathrm{o} = \frac{-3\rho}{(1+\rho)^{\frac{5}{2}}}, \tag{3}$$

$$\rho = \frac{s-b}{d}, \tag{4}$$

where $-\Psi_\mathrm{e}$ describes the v_x profile when the object is moving parallel to the array and Ψ_o when the object is moving orthogonal to the array ($\varphi = \pi/2$).

We extend this family of wavelets to also consider the velocity profile component orthogonal to the array, v_y. Here, Ψ_o describes v_y when the object is moving parallel to the array and Ψ_n when it is moving orthogonal to the array:

$$v_y = \frac{Wa^3}{2d^3}(\Psi_\mathrm{n}\sin\varphi + \Psi_\mathrm{o}\cos\varphi), \tag{5}$$

$$\Psi_\mathrm{n} = \frac{2-\rho^2}{(1+\rho)^{\frac{5}{2}}}. \tag{6}$$

A graphical representation of the wavelet family and velocity profiles can be found in Fig.1. At increasing distances, the velocity profiles decrease in magnitude, but also undergo spatial broadening [11]. The broadening is reflected in the minima, maxima, and zero crossings of the velocity profile; they displace further from the center of the profile, while the general shape remains.

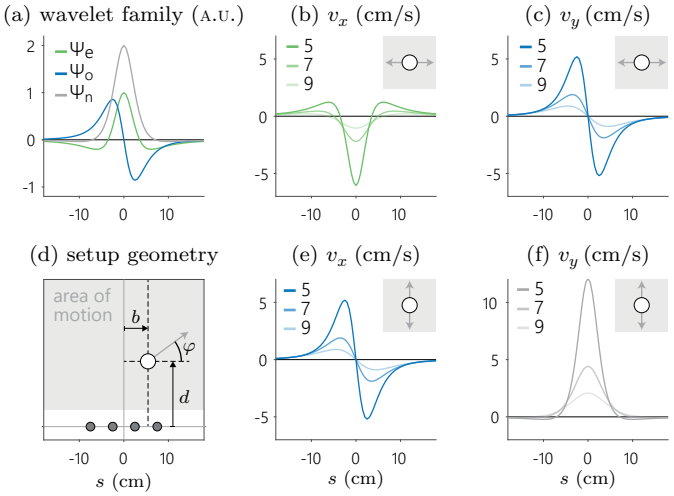

Fig. 1. Depiction of the wavelet family (a), the setup geometry (d), and example velocity profiles. The setup geometry (d) depicts the location of the four sensors (grey spheres) and an object (white) moving in a certain direction φ with respect to the array at coordinate (b, d). subfigures (b, c, e, f) show the expected velocity pattern for a vibrating object at 5, 7, and 9 cm distance.

C. Optical 2D sensing

Our sensor array consists of four novel, isotropic, all-optical, 2D-sensitive fluid flow sensors [15], which enables measuring a planar projection of the hydrodynamic environment. These sensors consist of a fluid force recipient sphere and a fiber support, constructed from four standard communication SMF-28 fibers.

The four fibers are each inscribed with a fiber Bragg grating (FBG) near the sensor base and have an associated distinct Bragg wavelength. The Bragg wavelength denotes a reflectance peak, which can be measured via an optical interrogator. When the sensor is deflected, the internal fibers stretch and compress, producing a measurable Bragg wave-

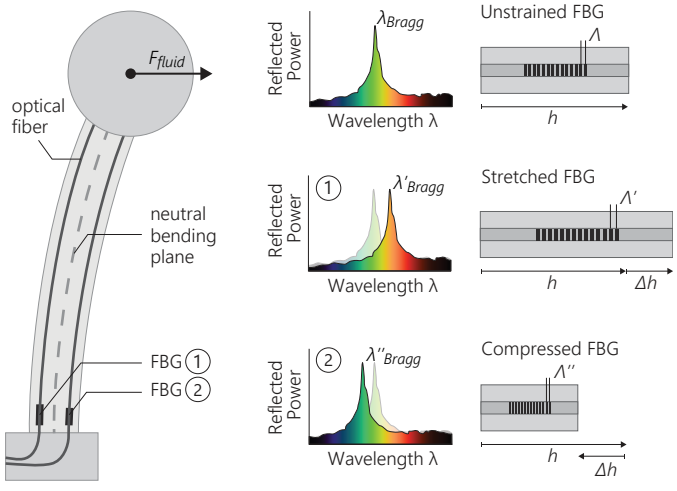

Fig. 2. Schematic overview of sensor design and sensing principles, adapted from [15]. When the sensor is deflected, opposite fiber cores will stretch and compress respectively, producing a shift in the measured Bragg wavelength.

length shift, see also Fig.2. The FBGs are also linearly affected by temperature, but this effect is smaller and can be factored out by using the wavelength shift difference between pairs of FBGs, since the temperature difference between FBGs in a sensor unit is negligible [16].

In [15] we show that this sensor design is isotropic, i.e. equally sensitive in both directions. Furthermore, a hydrodynamic model inspired by the fish neuromast provides an analytical frequency response that can be used to relate sensor deflection to local fluid velocity, taking into account both inertial and viscous drag fluid forces.

D. Processing methods

For both simulated and physical artificial lateral line arrays, several algorithms have been put forth to decode a velocity profile to retrieve the location of a dipole source. In [11] a continuous wavelet transform was proposed, based on the mother wavelets as described in section II-B. A data-matching approach where a measured excitation pattern is compared to a large set of templates was suggested by [17]. This template matching approach was later shown to be outperformed by Capon's beamforming algorithm [5]. More recently, artificial neural network architectures, including the Extreme Learning Machine, have been used to determine an object's location [8], [18] and orientation [6].

E. Neural network

To demonstrate the localization performance on a limited size data set with our array, we make use of an efficient single-layer feed-forward neural network, the Extreme Learning Machine (ELM) [19]. This type of neural network has a single hyper parameter, the size of the hidden layer, which allows for fast optimization while preventing over fitting. This type of neural network has shown the best performance for hydrodynamic object localization compared to more advanced neural networks [8].

III. Dipole object localization

In this experiment, we benchmark hydrodynamic imaging by the task of localizing a dipole source (i.e. vibrating object) positioned at discrete locations.

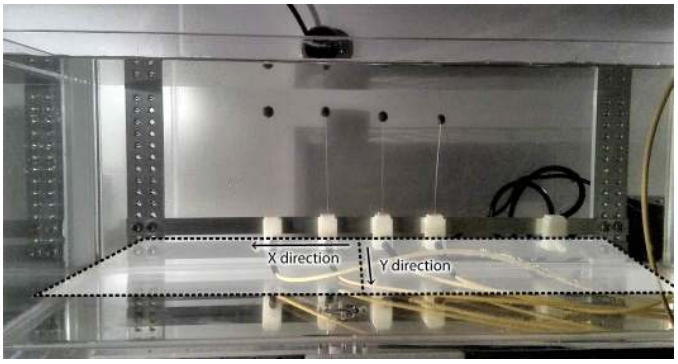

Fig. 3. Four sensors are mounted 3 cm from the back wall of a 25 × 50 cm testing tank. The stimuli are leveled with the fluid force recipient spheres during the experiments.

A. Setup

In our experimental setup, four sensors form an array of 14 cm, or artificial lateral line, at one side of a water tank measuring 25 × 50 cm, see Fig.3. The sensors are positioned 3 cm from the back wall via a guiding rail parallel to the long side of the tank. The drag force recipient spheres are leveled about 3 cm under the water surface. During all experiments, the object is leveled with the sensors. The Bragg wavelengths of the sensors are measured at 1 kHz using an optical interrogator (Micron Optics sm125, Atlanta, USA).

B. Methods

A B&K 4810 mini shaker is used in combination with a signal generator to vibrate the submerged sphere, 6 cm in diameter, at 8 Hz with a motion amplitude of 1 mm. We direct the motion towards the array ($\varphi = -\pi/2$), we therefore expect to see Ψ_o in the x-component of the measured velocity pattern and Ψ_n in the y-component (see section II-B).

For each location, we record 40 seconds of sensor data while the object is vibrating. Via a discrete Fourier transform, we obtain the magnitude of fluid flow at the stimulation frequency for the four sensors and 2 dimensions, reducing the sensor data to a vector of 8 points per location.

C. Results

Since the current array lacks the spatial resolution to properly assert the velocity profile, we first present the measured flow velocities per sensor rather than location. In Fig.4 we show the measured amplitudes for 11 lateral locations at three distance levels together with a parametric fit based on the expected wavelets. Especially for the profiles measured close to the array, the sensor readings correlate very well with theory. At further distances, both the effects of reduced amplitude and spatial broadening of the velocity patterns are present.

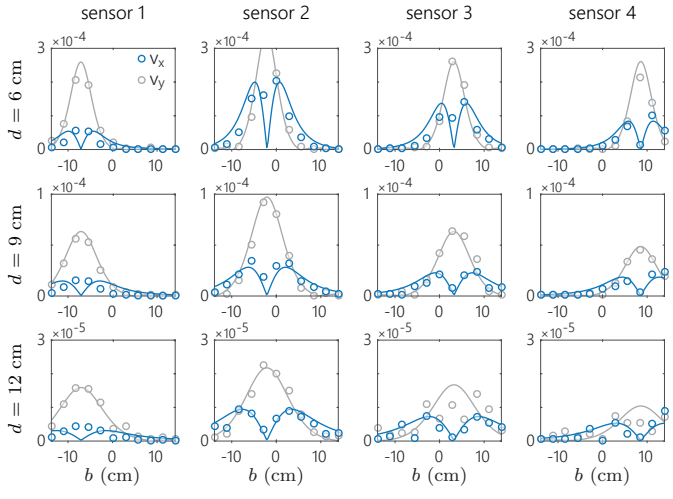

Fig. 4. For each sensor, the response magnitude (m/s) for 11 lateral positions b per distance d is shown. Note that for increasing distances, the y-axes are scaled as to make the spatial properties visible for decreasing magnitudes.

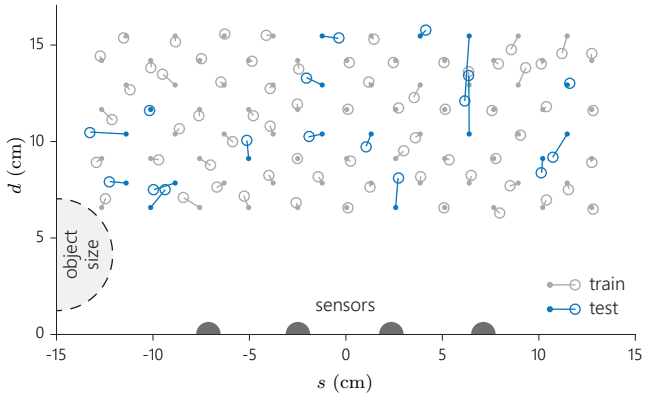

Fig. 5. Localization results for a single fold of the dipole localization benchmark. The estimated locations '○' are linked to their respective true location '●'. The distance error of the training set (gray) is slightly lower than the unseen test set (blue).

Finally, we trained an ELM neural network for localizing the object based on the sensor responses, the results of which are shown in Fig.5. Here, we used a 5-fold validation on 84 locations, where a random 80% portion of the measured locations is used for training while the remaining 20% is given to the neural network to predict. Therefore not all locations are used for training. The ELM hidden layer size was 1000.

We calculate the mean Euclidean localization error by combining the 5 folds and averaging the error distances of the 5 test sets and the 5 training sets. This error for the (unseen) test set was 1.3 cm, while the (seen) training set had a better estimate with an error of 0.45 cm. The ALL and ELM are therefore able to reconstruct locations from excitation patterns for unseen locations (Fig.5).

IV. Moving object localization

As was shown in [14], the velocity patterns resulting from motion with constant speed are, ignoring vorticity and other viscous effects, identical to those from dipole sources. However, the object is moving rather than vibrating, we therefore adapt the setup and apply different preprocessing steps before feeding the data to the ELM neural network for localizing the object.

A. Setup

For this bench marking task, the water tank setup is fitted with an Arduino controlled XY plotter (Makeblock) to enable an object to be moved in a straight path at constant height. Both the optical interrogator, which reads out the sensors, and the Arduino controller board are controlled through a Matlab script to allow for simultaneous stimulation and recording of sensor data. Furthermore, the Arduino board reports its location on preset intervals as to provide accurate training labels, i.e. annotated locations.

The object (6 cm diameter) is leveled with the sensors and moved at a constant speed of 7 cm/s, with a ramp up and down at the start and end of its motion. The sensor positions have been changed to form a slightly smaller array of 12 cm.

B. Preprocessing and validation

To determine valid preprocessing steps and the hyper parameter of the neural network, we first record a pilot data set of motion parallel to the array at six distances from 4 to 9 cm. This pilot data set consists of 10 repetitions of both forward and backward motion for each distance, so 120 runs in total. We use 5-fold stratified cross validation to validate the performance of the chosen settings.

We varied the hidden layer size between {1000, 1500, 2000, 2500}. Furthermore we varied a down sampling factor between 1 (no down sampling) to 53. Since this experiment produces time traces, we can take past detection into account. We implement this via feeding time windows to the ELM, rather than a single time step. To determine the optimal window length, we vary the history window size from 1 (no history) to 45. To make sure that the algorithm can provide timely output, we limit the amount of effective history (Δt per frame after down sampling $\times$ history size) to 500 ms.

From these settings, the estimator with the lowest test error has a hidden layer size of 1500, down samples by averaging 37 samples and takes 13 history steps as input and therefore requires a history buffer of 481 ms.

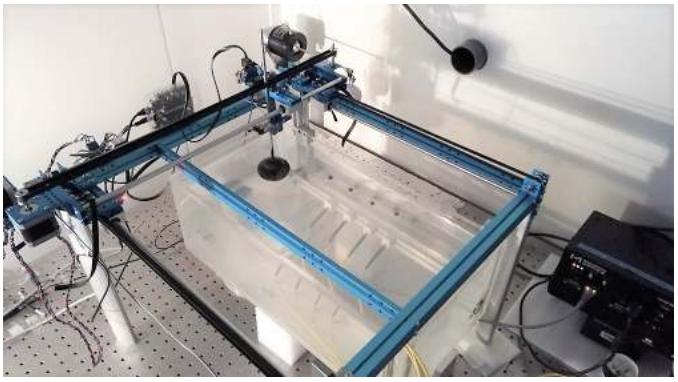

Fig. 6. Adapted setup for moving the object with the 2D plotter (blue). The optical interrogator is visible in the bottom right corner.

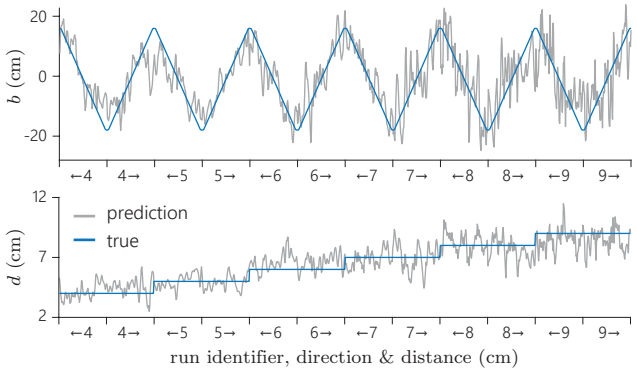

Fig. 7. Prediction and true location of the object for the pilot data test set for one fold. Shown here is the concatenation of 12 different run cases.

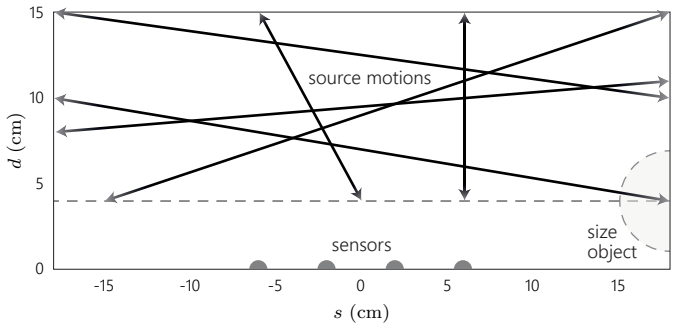

Fig. 8. A selection of the paths in the data set in a 36 × 11 cm bounded area. All motions are straight and edge-to-edge within the bounding box. The gradient on the motion arrows resemble the ramp up and down.

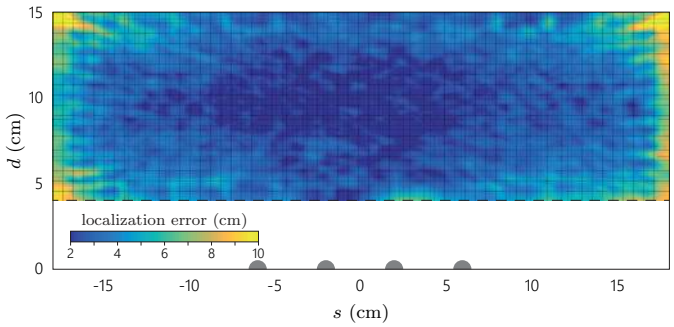

Fig. 9. Meshed interpolation of the Euclidean localization error with respect to the true location of the object. While the edges display an increase in estimation error, a large central area in front of the array has an error comparable to the object radius and could be interpreted as correct localization.

The output on the test set of a single fold of the optimal estimator is shown in Fig.7. Here we observe that the prediction of the x-coordinate (b) is of better quality than the y-coordinate (d) prediction, which can be caused by the former having more variation in the pilot data set. Another observation is that the prediction performance decreases over the distance d, which aligns with the fact that velocity patterns from objects at distances further away also have a lower signal to noise ratio.

C. Methods

For the final benchmark experiment, the XY plotter is instructed to move the object back and forth 5 times across 313 straight paths within an x,y bounding box of 36 × 11 cm. Fig.8 indicates this bounding box and shows a small selection of the used paths. Here, b was divided in 13 points from -18 to 18 cm, and d was divided in 12 points from 4 to 15 cm.

The set of motions was constructed from all points of one side to all points on its opposing side. The total data set consists of 3130 runs. With this set, we apply 5-fold stratified cross validation (four of the recorded sets of motions are used for training; the fifth set is used for testing).

D. Results

The averaged Euclidian error on the whole test set is 3.3 cm (see also Fig.9) and 3.2 cm for training. The localization error is comparable to the object radius and inter-sensor distance, but other relative interpretations are possible. Furthermore, the very small difference between the training and testing error indicates that there there is very little over fitting taking place.

These results indicate that moving object localization is feasible with an all-optical ALL of four sensors.

V. Discussion

We first showed that the 2D velocity profiles as measured by the four-sensor artificial lateral line (ALL) agree with those derived from a hydrodynamic model. Even though the sensors are not equally sensitive, the spatial variations such as wavelet broadening, zero crossings and maxima are clearly present in the measured data. Based on the sensitivity of the individual sensors, these spatial variations are progressively obscured at further distances, as expected.

The first benchmark test for hydrodynamic imaging was to localize a vibrating sphere. Using a small dataset (< 100 samples) of discrete object locations, we were able to show that an extreme learning machine (ELM) neural network can be easily trained to reliably predict an object's location based on the amplitudes of the excitation profiles. The mean Euclidian prediction error on the test set with 67 trained locations per fold was 1.3 cm in a bounded area of 27 × 11 cm. In a different dipole localization task [18], they achieved an average localization error of 0.28 cm with 90 training points and 4 enabled sensors in a 18 × 9 cm bounded area with a stronger source. With 50 training points, they achieved an average error of 0.4 cm. Between our area being larger, using a lower intensity dipole source, and the vibration direction being different, it is difficult to conclude which algorithm or array performs best based on the current experiment.

From the ELM and preprocessing optimization for moving objects, we found that considering past perceived excitation patterns helps in increasing localization performance. The most influential factor was not the amount of past inputs, but rather the effective amount of history taken into account. This makes sense from the point of view that excitation patterns not only encode location, but also direction: the object's direction remains the same throughout a path of motion. Data sets with other, non-straight motions might therefore call for taking a shorter amount of history into account.

The final performance on the second benchmark test came to an average Euclidian localization error of 3.3 cm in a bounded area of 36 × 11 cm. This task is somewhat harder to achieve, since there's no direct mapping from location to perceived excitation pattern; the object passed some points several times, but from different angles. To the best of our knowledge, there are no direct experimental comparisons for this task in the literature. Simulation results with 16 sensors and an ELM [6] indicate that an error of 0.9 cm is the lower bound for a 12 cm array in noiseless conditions. Considering that our error of 3.3 cm is in the same order of magnitude, it performs quite well.

The current sensors have shown to be sufficiently sensitive for the hydrodynamic stimuli used in this study, but tied with their sensitive nature is that the sensors are fragile. In the current environment we controlled the object's position, but for future deployments these sensors could be fitted in protective housings, which may also increase the robustness to noise and DC offsets for dynamical signals [20].

Another step to improve the accuracy concerns the number of sensors and the array geometry. As shown in [8], the number of sensors greatly affects localization performance; a first step would be to increase the spatial resolution of the array. Here, the inter-sensor distance can also have an influence [10]. Other sensor configurations than the bio inspired equally spaced line might also be improve the performance.

Furthermore, given that the predicted location for a moving object is quite noisy (e.g. Fig.7), post processing methods such as particle filters or median filtering could be considered for stabilizing the network output.

VI. Conclusion

Both benchmark tests were successful in the sense that object localization was possible using the novel, all-optical, 2D artificial lateral line (ALL) whether the object was vibrating at discrete positions or unidirectionally moving through a bounded area. We consider this result encouraging, even more so when considering that these results only stem from a relatively sparse four-sensor artificial lateral line.

Summarizing, our results show that the current sensor design and ALL implementation is very well suited for hydrodynamic imaging of moving and vibrating objects. The current sensor design, results, and analysis provide promising future developments.

Acknowledgment

We would like to thank Eize Stamhuis, Dennis Worst, and Jonathan Morton for facilitating this study.

References

[1] S. Dijkgraaf, "The Functioning and Significance of the Lateral-Line Organs," Biological Reviews, 38(1), pp. 51–105, 1963.

[2] G. Liu, A. Wang, X. Wang, and P. Liu, "A review of Artificial Lateral Line in sensor fabrication and bionic applications for robot fish," Applied Bionics and Biomechanics, pp. 4732703, 2016.

[3] H. Herzog, S. Steltenkamp, A. Klein, S. Tätzner, E. Schulze, and H. Bleckmann, "Micro-machined flow sensors mimicking lateral line canal neuromasts," Micromachines, 6(8), pp. 1189–1212, 2015.

[4] A. Ahrari, H. Lei, A. M. Sharif, K. Deb, and X. Tan, "Design optimization of an artificial lateral line system incorporating flow and sensor uncertainties," Engineering Optimization, 49(2), pp. 328–344, 2017.

[5] Y. Yang, N. Nguyen, N. Chen, M. Lockwood, C. Tucker, H. Hu, H. Bleckmann, C. Liu, and D. L. Jones, "Artificial lateral line with biomimetic neuromasts to emulate fish sensing," Bioinspiration & Biomimetics, 5(1), pp. 016001, 2010.

[6] B. J. Wolf, and S. M. van Netten, "Training submerged source detection for a 2D fluid flow sensor array with extreme learning machines," in Eleventh International Conference on Machine Vision (ICMV 2018), International Society for Optics and Photonics, in press.

[7] Y. Yang, J. Chen, J. Engel, S. Pandya, N. Chen, C. Tucker, S. Coombs, D. L. Jones, and C. Liu, "Distant touch hydrodynamic imaging with an artificial lateral line," Proceedings on the National Academy of Sciences, 103(50), pp. 18891–18895, 2006.

[8] L. H. Boulogne, B. J. Wolf, M. A. Wiering, and S. M. van Netten, "Performance of neural networks for localizing moving objects with an artificial lateral line," Bioinspiration & Biomimetics, 12(5), pp. 056009, 2017.

[9] S. Coombs, and J. C. Montgomery, "The enigmatic lateral line system," in Comparative Hearing: Fish and Amphibians, Vol. 11, R. R. Fay, and A. N. Popper, Eds. New York: Springer New York, 1999, pp. 319–362.

[10] A. T. Abdulsadda, and X. Tan, "Nonlinear estimation-based dipole source localization for artificial lateral line systems," Bioinspiration & Biomimetics, 8(2), pp. 26005, 2013.

[11] B. Curcic-Blake, and S. M. van Netten, "Source location encoding in the fish lateral line canal," Journal of Experimental Biology, 209(8), pp. 1548–1559, 2006.

[12] A. M. K. Dagamseh, T. S. J. Lammerink, M. L. Kolster, C. M. Bruinink, R. J. Wiegerink, and G. J. M. Krijnen, "Dipole-source localization using biomimetic flow-sensor arrays positioned as lateral-line system," Sensors and Actuators A: Physical, 162(2), pp. 355–360, 2010.

[13] J. Goulet, J. Engelmann, B. P. Chagnaud, J. M. P. Franosch, M. D. Suttner, and J. L. van Hemmen, "Object localization through the lateral line system of fish: theory and experiment," Journal of Comparative Physiology A, 194(1), pp. 1–17, 2007.

[14] J. M. P. Franosch, A. B. Sichert, M. D. Suttner, and J. L. van Hemmen, "Estimating position and velocity of a submerged moving object by the clawed frog Xenopus and by fish—A cybernetic approach," Biological Cybernetics, 93(4), pp. 231–238, 2005.

[15] B. J. Wolf, J. A. S. Morton, W. M. MacPherson, and S. M. van Netten, "Bio-inspired all-optical artificial neuromast for 2D flow sensing," Bioinspiration & Biomimetics, 13(2), pp. 026013, 2018.

[16] A. Fender, W. N. MacPherson, R. R. Maier, J. S. Barton, D. S. George, R. I. Howden, and R. Suo, "Two-axis accelerometer based on multicore fibre Bragg gratings," In Third European Workshop on Optical Fibre Sensors, Vol. 6619, International Society for Optics and Photonics, 2007, pp. 66190Q.

[17] S. Pandya, Y. Yang, D. L. Jones, J. Engel, and C. Liu, "Multisensor processing algorithms for underwater dipole localization and tracking using MEMS artificial lateral-line sensors," EURASIP Journal on Advances in Signal Processing, 2006, pp. 199–199, 2006.

[18] A. T. Abdulsadda, and X. Tan, "An artificial lateral line system using IPMC sensor arrays," International Journal of Smart and Nano Materials, 3(3), pp. 226–242, 2012.

[19] G. B. Huang, Q. Y. Zhy, and C. K. Siew, "Extreme learning machine: theory and applications," Neurocomputing, 70(1-3), pp. 489–501, 2006.

[20] Y. Yang, A. Klein, H. Bleckman, and L. Chang, "Artificial lateral line canal for hydrodynamic detection," Applied Physics Letters, 99(2), pp. 023701, 2011.